Zentrum für Technomathematik
Fachbereich 3 – Mathematik und Informatik

UNIVERSITÄT BREMEN

An ALE FEM for solid-liquid phase transitions with free melt surface

Eberhard Bänsch   Jordi Paul

Alfred Schmidt

Report 10–07

An ALE FEM for solid-liquid phase transitions with free melt surface

Eberhard Bänsch   Jordi Paul   Alfred Schmidt

September 3, 2010

Abstract

A finite element method is introduced which is capable to simulate the melting of solid material with a free melt surface. Especially in a micro scale situation, the free capillary surface and its interplay with the solid-liquid interface play an important role. The method is applied to the engineering process of melting the tip of a thin steel wire by laser heating. The mathematical system comprises heat conduction, radiative boundary conditions, and solid-liquid phase transition as well as the fluid dynamics in the liquid region and a free capillary surface. A sharp interface mesh–moving method (complemented by occasional remeshing) is used to track the liquid/solid interface as well as the capillary free boundary.

1   Introduction

We study the temperature-driven melting and solidification of material with a free capillary melt surface. The most important aspect of this process is the interplay of two free moving boundaries, the solid-liquid interface and the capillary free boundary of the melt. Both free boundaries are connected at a triple line, where the capillary surface meets the solid boundary. The movement of this triple line is an important aspect of the overall process, both from the modeling and the numerical point of view.

Especially for small dimensions (around $1mm$ or less), the capillary forces at the melt surface get dominant compared to other influences like gravity, and it is possible to melt a relatively large amount of material, while the process and geometry stay in a stable configuration. We describe a numerical method that is able to compute both geometric and flow aspects for the dynamic process in a stable manner.

The two main aspects, the solid-liquid phase transition and the liquid flow with a capillary boundary condition, are already intensively studied separately, and numerical methods for the approximation of solutions have been known for years. The solid-liquid phase transition can be modeled (mathematically and numerically) by various versions of the Stefan problem,

see for example [14, 19]. Viscous free surface flows are modeled by the Navier-Stokes equations with capillary boundary conditions [8].

The coupled problem, in particular with a free capillary surface, is studied much less. Some aspects are included in models for Czochalsky growth of semiconductor crystals, where the dimensions are relatively large [16]. The solidification of melt drops on a surface was studied in [2] by a simple model with a planar interface. Techniques using isotherms as coordinates (like the Isotherm Migration Method [12]) have successfully been applied to steady 2D cases, but are restricted to simple geometries and isotherm shapes [1, 17]. Anode melting was studied for example in [3], where the fluid flow in the liquid phase is neglected and a simplified 1D approach for the shape of the computational domain is used, and in [4], using finite volume methods and a transformation to a rectangular computational domain. Multi phase field models are able to model the neighbourhood of a triple junction accurately with high resolution [15, 18], but usually without considering any flow effects.

Our model leads to a coupled system of Stefan and Navier-Stokes equations, see Section 2, where the solution of the Stefan problem defines the solid subdomain $\Omega_s(t)$ and the solution of the Navier-Stokes equations with capillary boundary determines the shape of the liquid subdomain $\Omega_l(t)$. In Section 3, an Arbitrary Lagrangian Eulerian Finite Element method is presented that is able to compute a numerical solution in a robust way. A 2D rotational symmetric version was implemented for the simulation of the melting of initially cylindrical geometries. Numerical results, presented in Section 4, demonstrate the stability of the method and its applicability even in a situation where a relatively large amount of the geometry is melted.
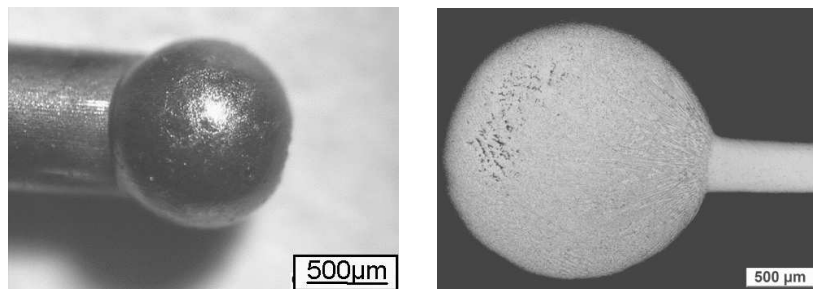

Figure 1: Material accumulation from experiments (source: BIAS).

This research is motivated and initiated by the engineering application of melting the end of thin wires by laser heating in order to accumulate material for a subsequent micro forming process [22], see Fig. 1. The Collaborative Research Centre 747 "Micro cold forming", located at the University of Bremen, studies such aspects of the production of micro components.

2 Mathematical model

In this section we present the continuum model, describing the laser heating, heat transport, the phase transition, and the fluid dynamical problem together with the free capillary surface condition. The crucial aspect here is given by the time dependence of the domains for the respective subproblems. Due to the wide range of temperatures, ranging from room temperature up to much more than the melting temperature of the material, radiative cooling will be considered in the model. Convective cooling on the boundary and Marangoni effects are neglected here in order to keep the model simple.
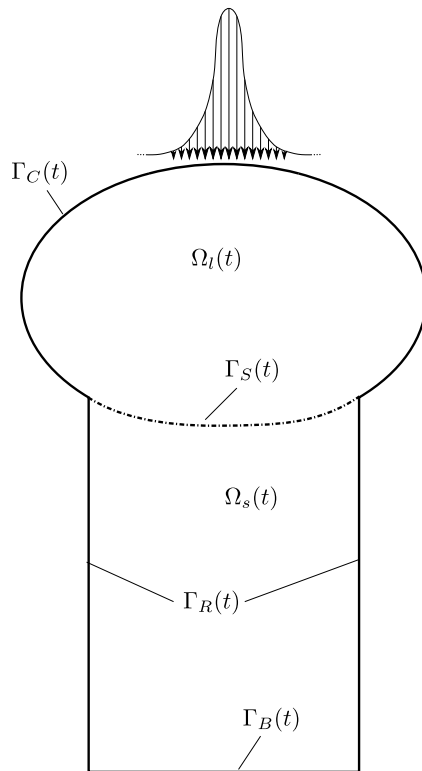

Figure 2: Sketch of the geometry.

Hereafter, we work in non–dimensional units. The derivation of the corresponding scalings are given in the Appendix. For $t \in [t_0, \bar{t}\,]$, let $\Omega(t) = \Omega_s(t) \cup \Omega_l(t) \cup \Gamma_S(t) \subset \mathbb{R}^3$ denote the time dependent domain, its solid and liquid subdomains and the solid-liquid interface at time t, respectively. Likewise, let $\Gamma_C(t)$ denote the free capillary surface, $\Gamma_R(t)$ the solid sides and Γ_B the bottom, see Fig. 2; $\nu(t, x)$ is the outer normal to $\Omega(t)$ or $\Omega_l(t)$ if taken on $\Gamma_S(t)$. For convenience we define the moving boundary $\Gamma_M(t) := \Gamma_C(t) \cup \Gamma_S(t)$.

The system is modeled by the Stefan problem in the whole domain for the

temperature $T : \Omega(t) \to \mathbb{R}$ and the incompressible Navier-Stokes equations with Boussinesq approximation in the liquid phase $\Omega_l(t)$ for the velocity field $\mathbf{u} : \Omega_l(t) \to \mathbb{R}^3$ and pressure $p : \Omega_l(t) \to \mathbb{R}$:

$$\partial_t \mathbf{u} + \mathbf{u} \cdot \nabla \mathbf{u} - \nabla \cdot \left(\frac{1}{Re} \mathbf{D}(\mathbf{u}) - p\mathbb{I} \right) = -\frac{Bo}{We}\mathbf{e}_2 + \frac{Gr}{Re^2}T\mathbf{e}_2 \quad \text{in } \Omega_l(t), \quad (1a)$$

$$\nabla \cdot \mathbf{u} = 0 \qquad\qquad\qquad \text{in } \Omega_l(t), \quad (1b)$$

$$\partial_t T + \mathbf{u} \cdot \nabla T - \frac{1}{RePr}\triangle T = 0 \qquad\qquad \text{in } \Omega_l(t), \quad (1c)$$

$$\partial_t T - \frac{q_{ls}}{RePr}\triangle T = 0 \qquad\qquad \text{in } \Omega_s(t), \quad (1d)$$

where $\mathbf{D}(\mathbf{u}) := \nabla \mathbf{u} + (\nabla \mathbf{u})^T$. Here, Re, Bo, We, Gr, and Pr denote the Reynolds, Bond, Weber, Grashof, and Prandtl numbers, respectively, and q_{ls} is a quotient of solid and liquid material parameters, see also the Appendix. Finally, $\mathbf{e}_2$ denotes the vertical unit vector.

On the capillary boundary $\Gamma_C(t)$, we impose:

$$\mathbf{u} \cdot \nu = \mathbf{V}_{\Gamma_C} \cdot \nu, \qquad\qquad (2a)$$

$$\sigma\nu = \frac{1}{We}\mathcal{K}\nu, \qquad\qquad (2b)$$

as boundary conditions, where $\mathbf{V}_{\Gamma_C}$ denotes the velocity of the free boundary, $\mathcal{K}$ the sum of the principle curvatures and $\sigma := \frac{1}{Re}\mathbf{D}(\mathbf{u}) - p\mathbb{I}$ is the stress tensor.

On the solid-liquid interface $\Gamma_S(t)$, conditions for $\mathbf{u}$, T and for the normal velocity of the interface $\mathbf{V}_{\Gamma_S}$ are prescribed:

$$\mathbf{u} \cdot \nu = (1 - q_\rho)\mathbf{V}_{\Gamma_S} \cdot \nu, \qquad\qquad (3a)$$

$$\mathbf{u} - \mathbf{u} \cdot \nu \, \nu = 0, \qquad\qquad (3b)$$

$$T = 0, \qquad\qquad (3c)$$

$$\frac{1}{RePr}\left[(\nabla T)_l - q_{ls}(\nabla T)_s \right] = \frac{q_\rho}{Ste}\mathbf{V}_{\Gamma_S}. \qquad\qquad (3d)$$

Eq. (3a) reflects mass balance with $q_\rho = \frac{\rho_s}{\rho_l}$ being the ratio of the densities of solid and liquid, respectively. Eq. (3d) is the Stefan condition, Ste being the Stefan number, and reflects thermal energy balance. On the outer boundary we need further thermal boundary conditions. External heating and radiative cooling conditions are imposed on $\partial\Omega(t) \setminus \Gamma_B$,

$$\begin{aligned} \frac{1}{RePr}\partial_\nu T &= La\, I_l + Em\left(T_a^4 - (T_m + T)^4 \right) \quad \text{on } \Gamma_C(t), \\ \frac{q_\kappa}{RePr}\partial_\nu T &= La\, I_l + Em\left(T_a^4 - (T_m + T)^4 \right) \quad \text{on } \Gamma_R(t), \end{aligned} \qquad (4)$$

4

with La and Em the laser absorption and emissivity parameters, T_a, T_m the ambient and melting temperatures, I_l the Gaussian laser intensity distribution function [21] and q_κ the ratio of thermal conductivity coefficients. At the bottom Γ_B we assume a non-flux condition,

$$\partial_\nu T = 0 \quad \text{on } \Gamma_B. \tag{5}$$

A typical initial condition for the experimental process would be given by $\Omega(t_0) = \Omega_0$ at room temperature, $T(\cdot, t_0) \equiv -1$, and thus $\Omega_l(t_0) = \emptyset$. However, as the sharp interface formulation given above does not contain any model for nucleation for a new phase, at $t = 0$ we start from a tiny liquid region $\Omega_l(0) \neq \emptyset$ and a corresponding temperature $T_0 = 0$ on $\Gamma_S(0)$ and vanishing velocity field,

$$T(x, 0) = T_0(x) \ \text{ on } \Omega(0), \quad u(x, 0) = 0 \ \text{ on } \Omega_l(0). \tag{6}$$

instead.

3 Numerical method

This section introduces the numerical method used to discretize system (1) – (6). A 2D rotational symmetric version of the problem is solved using NAVIER [8], a finite element solver for flow problems with capillary surfaces based on unstructured triangular grids. The Navier–Stokes equations are discretized by the Taylor-Hood element in space, i.e. piecewise quadratics for the velocities and piecewise linears for the pressure, and the fractional–step θ scheme in an operator splitting variant in time, see [11, 7]. As NAVIER is able to handle a time dependent capillary surface, the discretization of time dependent domains is already included into the code. It features a semi–implicit, variational treatment of the curvature terms in the Navier-Stokes equations and a decoupling of the flow from the geometry problem. The free capillary boundary is represented by isoparametric elements, i.e. piecewise quadratics, in combination with the variational treatment yielding a very precise discretization of the curvature terms.

For the Stefan subproblem, the solid-liquid interface is represented as an *interior boundary* of the triangulation, thus leading to sharp interface tracking. The heat equation on both subdomains is discretized by the fractional–step θ scheme in time, too, and piecewise quadratic elements in space.

The evolution of the time dependent domain $\Omega(t)$ is realized by discretizations of the boundary conditions (2a), (3d) and a corresponding *mesh moving* in the interior. An ALE (*Arbitrary Lagrangian Eulerian*) formulation is used for the PDEs on the time dependent domains, see for instance [13].

As $\Omega(t)$ and its subdomains $\Omega_l(t), \Omega_s(t)$ deform considerably during the process, mesh moving alone is not sufficient to maintain mesh quality. Thus a complete *remeshing* is performed when needed.

In the following, we describe this method in more detail.

3.1 Meshes, finite element spaces, and ALE formulation

Let $0 = t_0 < \cdots < t_N = \bar{t}$ be a partition of our time interval and set $\tau_n := t_{n+1} - t_n$. The time dependent domain $\Omega(t)$ is approximated by discrete, triangulated domains $\Omega^n \approx \Omega(t_n)$. In each time step, the new domain Ω^{n+1} is parametrized over Ω^n. An ALE formulation is based on this parametrization.

Since the geometric situation given is rotationally symmetric and the Reynolds numbers are rather small, we restrict ourselves to describing a corresponding rotationally symmetric method, i.e. $d = 2$. The full 3D method would be analogous.

We now describe the situation in more detail. For time interval (t_n, t_{n+1}), let the discrete domain $\Omega^n \approx \Omega(t_n)$ be given. Let $\mathcal{T}^n$ be a regular, conforming triangulation of Ω^n which respects the solid-liqid interface Γ_S^n, and Σ^n the corresponding partition of the exterior and interior boundaries $\Gamma^n := \partial\Omega^n \cup \Gamma_S^n$ into the edges of $\mathcal{T}^n$ on Γ^n,

$$\bar{\Omega}^n = \bigcup_{T \in \mathcal{T}^n} T, \quad \Gamma^n = \bigcup_{S \in \Sigma^n} S.$$

The liquid and solid subdomains Ω_l^n, Ω_s^n are given by the union of fully liquid resp. solid mesh elements in $\mathcal{T}_l^n, \mathcal{T}_s^n$. Finally, we define the discrete moving boundary by $\Gamma_M^n := \Gamma_C^n \cup \Gamma_S^n$.

For the definition of the Finite Element spaces on isoparametric meshes, let $\hat{T}$ denote the reference simplex in $\mathbb{R}^d$ and $\hat{S}$ the reference simplex in $\mathbb{R}^{d-1}$ (in the case $d = 2$, this means the unit interval). For each $T \in \mathcal{T}^n$ and for each $S \in \Sigma^n$ there exist invertible quadratic mappings

$$F_T : \hat{T} \to \mathbb{R}^d, \qquad F_T(\hat{T}) = T,$$
$$F_S : \hat{S} \to \mathbb{R}^{d-1}, \quad F_S(\hat{S}) = S.$$

Our discretization of the Stefan problem is realized using a piecewise quadratic finite element space over Ω^n for time step t^{n+1}, with temperature

$$T^{n+1} \in W^n := \{w_h \in C^0(\bar{\Omega}^n) : w_h \circ F_T \in \mathbb{P}_2 \, \forall T \in \mathcal{T}^n\}.$$

The Navier-Stokes equations are approximated by $\mathbb{P}_2/\mathbb{P}_1$ Taylor-Hood finite elements on Ω_l^n, i.e.

$$\mathbf{u}^{n+1} \in \mathbf{V}^n := \{v_h \in C^0(\bar{\Omega}_l^n)^d : v_h \circ F_T \in \mathbb{P}_2^d \, \forall T \in \mathcal{T}_l^n\},$$

$$p^{n+1} \in Q^n := \{q_h \in C^0(\bar{\Omega}_l^n) : q_h \circ F_T \in \mathbb{P}_1 \, \forall T \in \mathcal{T}_l^n\}.$$

The change of the domain shape is determined by the movement of the capillary surface Γ_C^n and the solid-liquid interface Γ_S^n, details are given below. In order to keep a good mesh quality, vertices on the solid boundary $\partial\Omega_s^n \backslash \Gamma_S^n$

are also allowed to move in tangential direction. All edge movements are parametrized via the corresponding finite element spaces, so the capillary surface and the phase boundary move piecewise $\mathbb{P}_2$, while it is sufficient to move the solid boundary piecewise $\mathbb{P}_1$. Accordingly we define the space of boundary movement $\mathbf{E}^n$,

$$\mathbf{E}^n := \left\{ \mathbf{e}_h \in C^0(\Gamma^n)^d : \mathbf{e}_h \circ F_S \in \begin{cases} \mathbb{P}_2^d \, \forall S \in \Sigma^n \cap \Gamma_M^n, \\ \mathbb{P}_1^d \, \forall S \in \Sigma^n \cap (\partial\Omega_s^n \setminus \Gamma_S^n) \end{cases} \right\}.$$

Given a boundary deformation $\Psi^{n+1} \in \mathbf{E}^n$, we need to deform the whole domain, and thus an extension operator $E : \mathbf{E}^n \to \mathbf{X}^n$, where

$$\mathbf{X}^n \subset \{v_h \in C^0(\bar{\Omega}^n)^d : v_h \circ F_T \in \mathbb{P}_2^d \, \forall T \in \mathcal{T}^n\}$$

is an appropriate finite element space with trace space $\mathbf{E}^n$. We take $\mathbf{X}^n$ to be piecewise linear in the interior of Ω_l^n, Ω_s^n and piecewise quadratic on Γ_M^n, although other choices are possible. The extension operator E will be defined by solution of a discrete Laplace equation,

$$\begin{aligned} (\nabla E(\Psi^{n+1}), \nabla x_h) &= 0 &&\forall x_h \in \mathbf{X}^n, \ x_h = 0 \text{ on } \Sigma^n, \\ E(\Psi^{n+1}) &= \Psi^{n+1} &&\text{on } \Sigma^n. \end{aligned} \tag{7}$$

With $\Upsilon^{n+1} := E(\Psi^{n+1})$ given, we set $\Omega_{n+1} = \Upsilon_{n+1}(\Omega_n)$, and the time discrete equations for velocity $\mathbf{u}^{n+1}$ and temperature T^{n+1} in the bulk are augmented by an additional ALE advection term

$$\mathbf{u}_{ALE} \cdot \nabla \mathbf{u}^{n+1} \quad \text{or} \quad \mathbf{u}_{ALE} \cdot \nabla T^{n+1},$$

respectively, with $\mathbf{u}_{ALE} = (\Upsilon_{n+1} - Id)/\tau_n$ accounting for the mesh movement.

3.2 Decoupling of geometry and PDEs in the bulk

Assume that $\Omega^n, \mathbf{u}^n, p^n, T^n$ for some $n \in \{0, \dots, N-1\}$ are known. We now decouple the computation of Ω^{n+1} and the bulk terms by assuming Ω^n as fixed and solving the equations on the fixed domain, where $(\mathbf{u}^{n+1}, p^{n+1})$ and T^{n+1} are again decoupled. The geometry is then updated according to the respective boundary conditions on the two moving boundaries Γ_C^n and Γ_S^n.

Except for the initial phase, where $\Omega_l(t) = \emptyset$, the typical geometric shape of $\Omega(t)$ is like in Fig. 3. Thus from one time step to the next one, it is convenient to solve the heat equation problem and then use the velocity $\mathbf{V}_{\Gamma_S}$ from the Stefan condition (3d) to update Γ_S. Likewise, the kinematic boundary condition (2a) can be used to define the update of Γ_C^n. The procedure for every substep n' of the fractional–step θ scheme is then as follows:
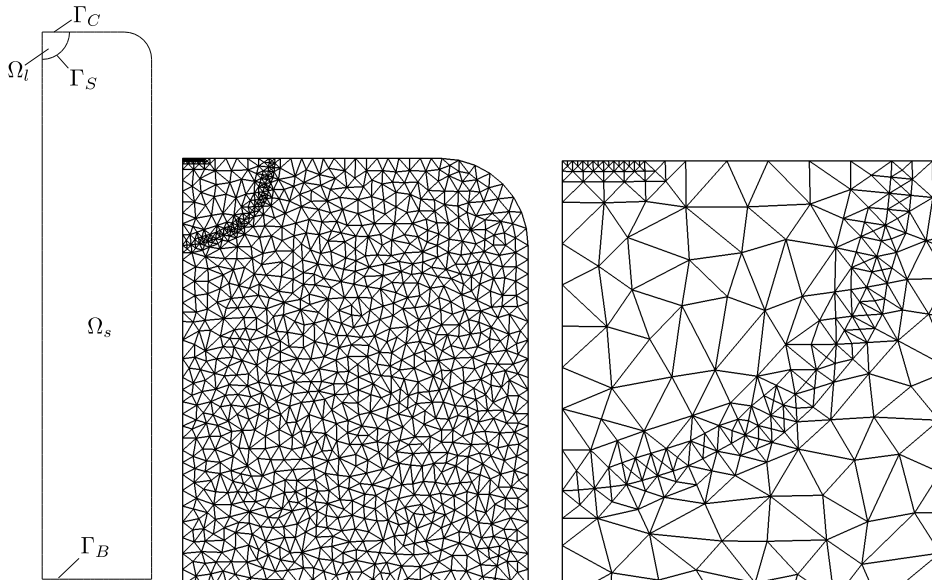
Figure 3: Typical form of Ω^0 (left) and the triangulation near the top (middle and right).

1. Solve the Navier-Stokes equations (meaning a quasi-Stokes or Burgers problem, depending on the fractional step in the θ splitting scheme, see [11]) on the fixed domain $\Omega^{n'}$ using $T^{n'}$ in the buoyancy term in (1a), giving $\mathbf{u}^{n'+1}$. The virtual position of the new free boundary enters in the equation as a stabilizing term, see [6, 8] for details.

2. Calculate $T^{n'+1}$ on the fixed domain $\Omega_l^{n'} \cup \Omega_s^{n'}$ by treating $\Gamma_S^{n'}$ as internal Dirichlet boundary and using $\mathbf{u}^{n'+1}$ in the convection term in equation (1c).

3. Use the kinematic boundary condition from (2a) and the Stefan condition from (3d) to obtain the boundary deformation $\Psi^{n'+1}$, see below. (Alternatively, this can also be done just once per full timestep, namely after the last fractional step. In this case, n' in the geometry update is understood as said timestep.)

We now specify how to derive the geometry update $\Upsilon^{n'+1} : \Omega^{n'} \to \Omega^{n'+1}$ from the boundary conditions. As $\mathbf{u}^{n'+1}$ and $T^{n'+1}$ are known after step 2 of the procedure, we can define the new boundary position $\Psi^{n+1} \in \mathbf{E}^n$ by

its nodal values at boundary nodes x,

$$\Psi^{n'+1} : \Gamma^{n'} \to \mathbb{R}^3,$$

$$\Psi^{n'+1}(x) := id_{\Gamma^{n'}} + \begin{cases} \mathbf{u}^{n'+1}(x), & x \in \Gamma_C^{n'} \setminus \Gamma_S^{n'} \\ \mathbf{V}_{\Gamma_S^{n'}}^{n'+1}(x), & x \in \Gamma_S^{n'} \\ 0 & x \in \partial\Omega^n \setminus \Gamma_M^{n'} \end{cases}, \tag{8}$$

$$\partial\Omega^{n'+1} := \Psi^{n'+1}(\Gamma^{n'}).$$

Using the extension operator E from Section 3.1, we obtain the update

$$\Upsilon_{n'+1} = E(\Psi^{n'+1}), \quad \Omega^{n'+1} = \Upsilon_{n'+1}(\Omega^{n'}).$$

As the definition of $\Psi^{n'+1}$ does not allow for movement of boundary nodes in the solid phase, leading to a rapid deterioration of the triangles containing the triple point, the boundary conditions for E from Eq. (7) are relaxed to allow for tangential movement on $\Gamma_R^{n'}$:

$$E(\Psi^{n'}) = \Psi^{n'} \quad \text{on } \partial\Omega^{n'} \setminus \Gamma_R^{n'},$$

$$E(\Psi^{n'}) \cdot \nu = 0 \quad \text{on } \Gamma_R^{n'}.$$

A few remarks on the above method:

1. In practice, the grid updates are quite small, so taking smoothing by a discrete Laplace operator like in Eq.(7) as extension is sufficient, see [6]. Note that the ALE convection term $\mathbf{u}_{ALE}$, accounting for the mesh moving, is given by

$$\mathbf{u}_{ALE} = \dot{\Upsilon}.$$

2. The term $[(\nabla T)_l - q_{ls}(\nabla T)_s]$ is discontinuous across element boundaries on $\Gamma_S^{n'}$ in general because the temperature is continuous only. Thus the L^2–projection $\mathbf{V}_{\Gamma_S^{n'}}^{n'+1}$ of the jump term to the space of piecewise quadratic functions on $\Gamma_S^{n'}$ is used. This matches well with the update of Γ_S^n arising from Eq. (8) and the velocity boundary condition from Eq. (3a).

3. The phase boundary is a non–material surface, meaning that its movement is not related or influenced by the movement of the material (physical) points on it at any given instant. In fact, the mesh and the material points move independent of each other, as shown in Fig. 4. This in turn means that the movement of $\Gamma_S^{n'}$ does not introduce any singularities to the boundary conditions on $\Gamma_C^{n'}$ and $\Gamma_S^{n'}$.

4. As the triple point x_t itself is non–material, it is moved with the grid on $\Gamma_S^{n'}$, see also Fig. 4. It is clear that x_t can only move tangentially in $\partial\Omega^{n'}$, so the full update $\tilde{x}_t(t_{n'+1}) = x_t(t_{n'}) + \mathbf{V}_{\Gamma_S^{n'}}^{n'+1}(x_t(t_{n'}))$ is suitably projected to the isoparametric surface $\partial\Omega^{n'}$ to obtain $x_t(t_{n'+1}) = \Psi^{n'+1}(x_t(t_{n'}))$.

5. Since the update of $\Gamma_C^{n'}$ is defined by $\mathbf{u}_{|\Gamma_C^{n'}}$, large tangential velocities would lead to a quick distortion of the mesh. The same problem may arise from the movement of $\Gamma_S^{n'}$. In order to avoid this, a *curve smoothing* is used that equilibrates the boundary node distribution by moving boundary nodes along the geometry.
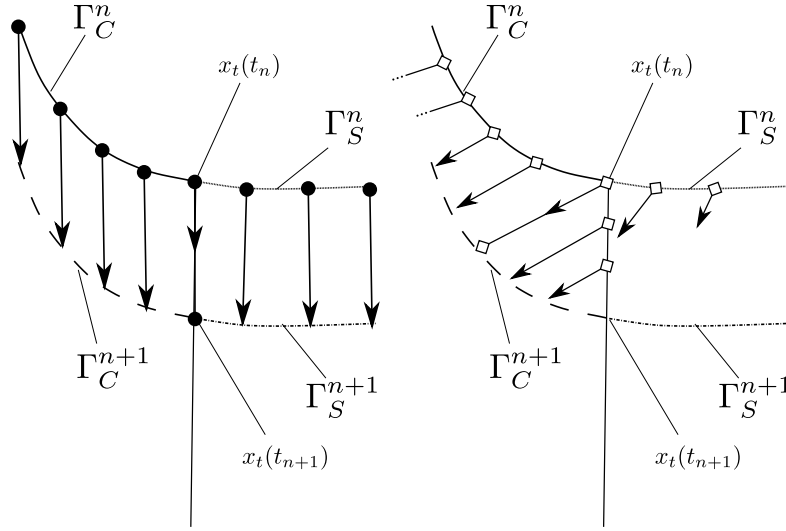

Figure 4: Movement of the grid points $\bullet$ (left) and of some arbitrary material points $\diamond$ (right) on $\Gamma_C \cup \Gamma_S$.

3.3   Remeshing

As the domain evolves, the mesh is deformed by the movement of Γ_C and Γ_S. Especially when one of the subdomains Ω_l, Ω_s is small compared to the other, the change in relative sizes of the subdomains Ω_l, Ω_s can be quite large. A good quality of the mesh cannot be guaranteed by a refinement/mesh moving strategy alone, thus a complete remeshing of the whole domain is necessary.

Remeshing is performed either in fixed time intervals (e.g. every N time-steps), or when a certain condition for the maximum angle of a triangle (i.e. $140°$) is violated, or when the volume of a triangle has changed considerably (i.e. a factor of five).

To implement such a remeshing, we use the 2D mesh generator TRIAN-GLE [20], with additional refinement performed using NAVIER's own refinement algorithms [5] to guarantee certain element sizes at selected boundaries.

Remeshing (i.e. at timestep n) is done as follows:

1. Write out $\partial\Omega^n$ and Γ_S^n as planar straight line graph (PSLG), let TRI-ANGLE generate the new grid and re-import it into NAVIER.

2. Refine the new mesh near $\tilde{\Gamma}_S^n$ and $\tilde{\Gamma}_C^n$, i.e. so that certain edge lengths are not exceeded.

3. Correct the new $\tilde{\Gamma}_C^n$ to obtain the new, piecewise quadratic Γ_C^n.

   Since TRIANGLE can only generate straight simplices, all edge midpoints and any newly inserted nodes lie on straight edges, although the boundary was piecewise quadratic before, resulting in (relatively) large oscillations of the free surface. Thus the boundary has to be corrected after remeshing. This is achieved by projecting edge midpoints and newly inserted nodes of the new (straight) mesh onto the old geometry (see Fig. 5).
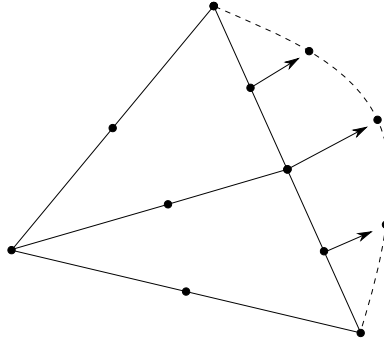

Figure 5: A triangle was refined during remeshing. Points lying on the straight boundary edge are projected to their appropriate positions on the old (curved) edge (dashed line).

4. Transfer the old data ($\mathbf{u}^n, T^n$ and grid velocities for the ALE formulation) onto the new grid by appropriate projections onto the corresponding finite element space.

   The calculation of the projections requires the evaluation of the old functions on the new grid. For this, an implementation of a highly efficient algorithm from [10] is used, which is based on a stack structure exploiting the neighbouring relations of elements in the mesh.

   Because of the remeshing, the velocity and pressure spaces change at time step n. Thus an interpolated or simple L^2 projection of the velocity from the old mesh is no longer discretely divergence free on

the new mesh in general. Using these velocities would result in strong erroneous pressure peaks. This has to be cured by projecting the old $\mathbf{u}^n$ directly onto the space of discretely divergence free function on the new mesh via the L^2 inner product, see [9].

4   Numerical results

In this section, we present numerical results obtained by the discussed method. Simulations were run with different space discretizations, coefficients $La \in [2 \cdot 10^3, 10^4], Em \in \{0, \ 9 \cdot 10^{-4}\}, q_\rho \in \{0, \ 1.125\}$ and the rest of the parameters as given in the Appendix. When not stated otherwise, the simulations were done with $La = 10^4$ (corresponding to approx. 120W), $Em = 9 \cdot 10^{-4}$, $q_\rho = 1.125$, a time step size of $2 \cdot 10^{-4}$ (5000 timesteps correspond to 100ms), and a domain corresponding to a wire of 1mm diameter.
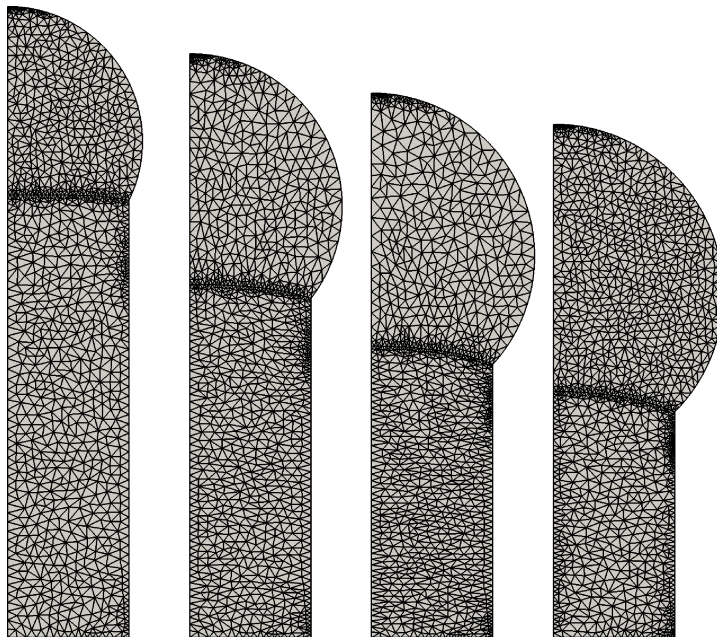
4.1   Melting a wire end

Figure 6: Domain and mesh at t_{10000} for parameters $La = 4 \cdot 10^3, 6 \cdot 10^3, 8 \cdot 10^3, 10^4$ (from left to right).

At the start of the simulation, the phase boundary moves quite fast due to the rapid heating by the laser and therefore expands quickly. A relatively frequent remeshing is needed at this stage. As the domain evolves and the phase boundary moves further away from the heated boundary, the phase

transformation and thus the mesh moving and deforming slows down, which results in a relatively stable mesh quality without too frequent remeshings. Due to the small length scale, surface tension is dominant, so the liquid subdomain remains stable even for relatively large melt regions (see Fig. 6).
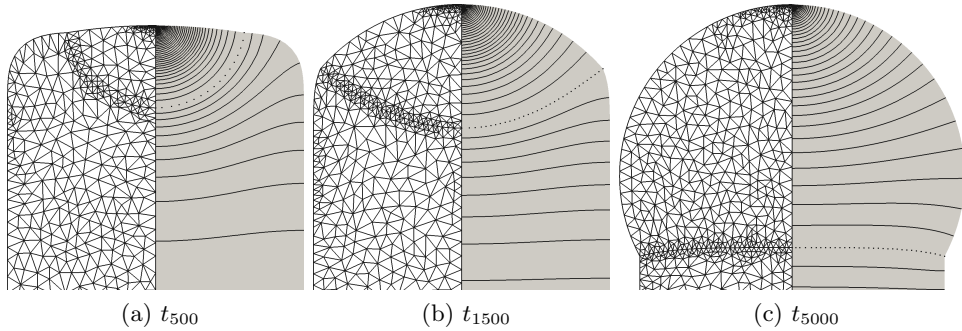

(a) t_{500} (b) t_{1500} (c) t_{5000}

Figure 7: Grid and domain with temperature isolines at different timesteps.

Fig. 7 shows the domain at different timesteps, along with the grid and temperature isolines. For $n = 500$, the relatively large deformation of the grid shortly before a remeshing operation can be seen, while the other two pictures show how the domain typically looks like if the phase boundary has slowed down.

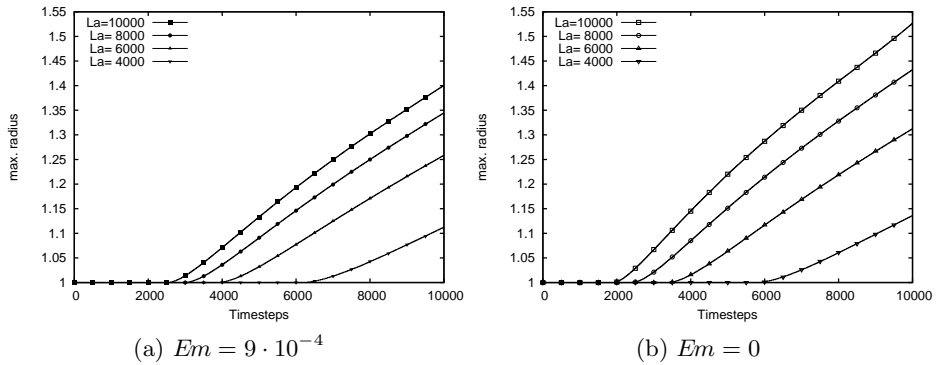(a) $Em = 9 \cdot 10^{-4}$ (b) $Em = 0$

Figure 8: Maximum radius of the liquid region over time with and without radiation.

Fig. 8 shows the maximum radius of the liquid region over time for different parameters La, as this is of interest for the application. The radius stays at 1 until the domain reaches the half–sphere configuration and increases afterwards as the liquid region expands further. Energy loss by radiation has a significant impact on the radius of the final shape.

The boundary conditions on Γ_S^n have a significant impact on the flow

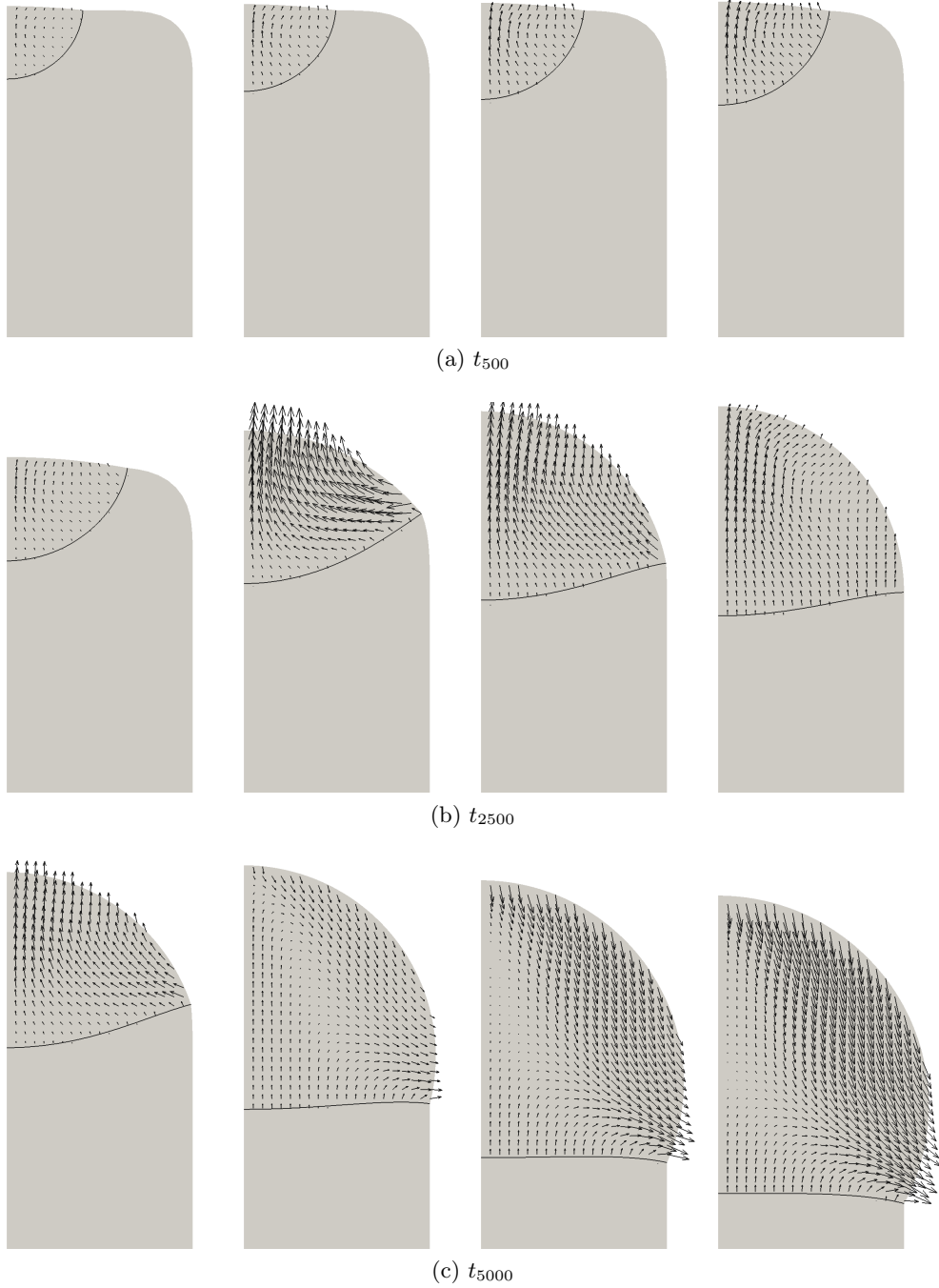(a) t_{500}

(b) t_{2500}

(c) t_{5000}

Figure 9: Domain and velocity field at different timesteps for parameters $La = 4 \cdot 10^3, 6 \cdot 10^3, 8 \cdot 10^3, 10^4$ (from left to right).
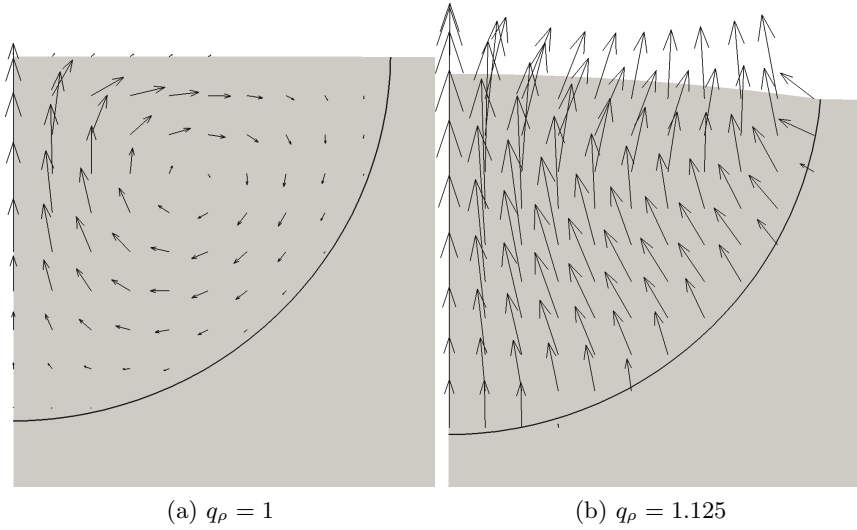
14

(a) $q_\rho = 1$ (b) $q_\rho = 1.125$

Figure 10: The flow field at t_{250} with different values q_ρ.

field. If the mass density in the liquid is lower than in the solid (meaning $q_\rho > 1$), equation (3a) is an inhomogeneous Dirichlet condition. At the start of the simulation, this boundary condition dominates the flow field, while for $q_\rho = 1$ the flow field is dominated by free convection (see Fig. 10).
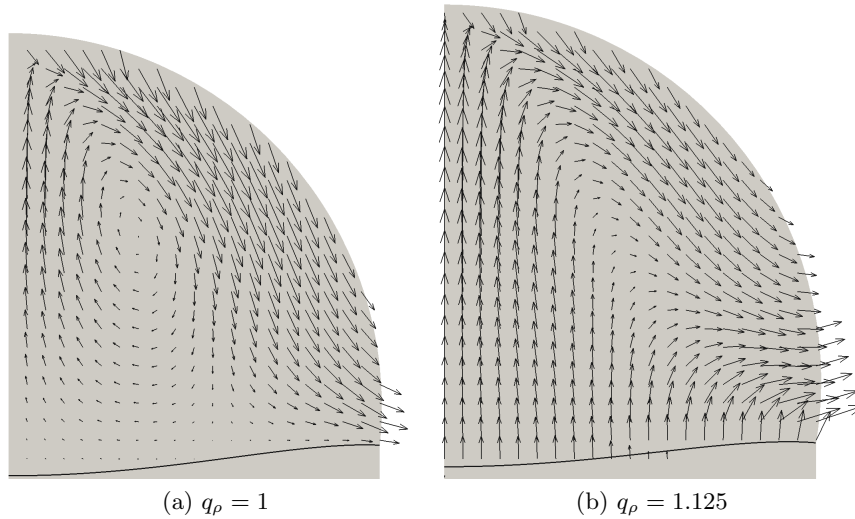

(a) $q_\rho = 1$ (b) $q_\rho = 1.125$

Figure 11: The flow field at t_{3000} with different values q_ρ.

After the liquid phase has reached a half–sphere configuration, the motion of the free capillary surface dominates the flow field. As the influence of convection is lower than the influence of the Dirichlet condition, this happens

sooner for the case $q_\rho = 1$. Even though the liquid phase enlarges considerably, the geometry stays stable and occasional remeshing keeps the grid from deteriorating. A comparison of the evolution for different parameters La can be found in Fig. 9.

Due to the explicit treatment of the phase boundary movement, a CFL condition restricts the space and time distretization parameters, but not significantly beyond the usual bounds for the solver. Our numerical experience is that refinement at the phase boundary is not needed to ensure its stability in the mesh moving method.

4.2   Remeshing issues

The remeshing introduces some technical problems. If the temperature is transferred to the new grid by L^2 projection, the gradients at the phase boundary are not preserved and generally do not match with the current phase boundary velocity. This leads to oscillations in the phase boundary velocity, but these decay quickly (see left part of Fig. 12) and have no significant influence on the stability.
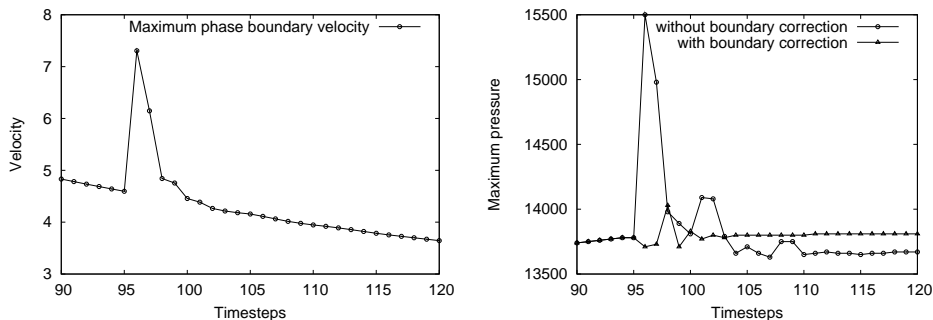

Figure 12: The maximum phase boundary velocity over time (left) and the maximum pressure with and without boundary correction (right) near a timestep with remeshing.

Another difficulty is presented by the free capillary surface. During remeshing, boundary edges might be refined, so that the old shape does not correspond to an equilibrium configuration according to the new discrete curvature. This can lead to capillary waves running over the free surface, which in turn have an influence on the velocity and the pressure.

To illustrate the impact of a mismatch of geometries, the boundary correction from Section 3.3 is omitted in the remeshing process, causing all edges in the domain to be straightened out. The resulting peak in the maximum pressure and a comparison to the case with boundary correction (in which the effect is due to the refinement of the capillary boundary) can be found in Fig. 12.
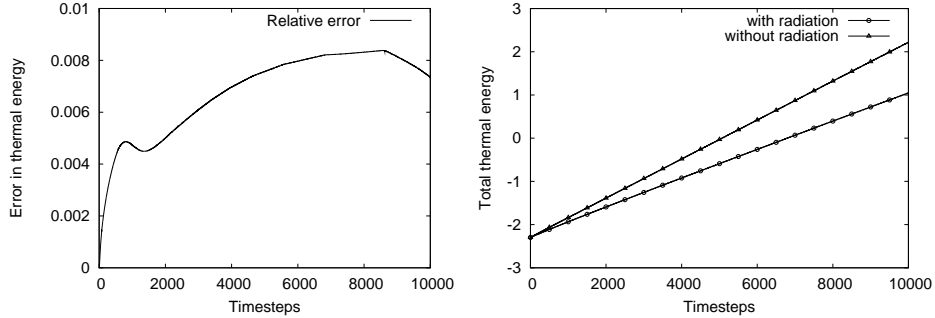
16

4.3 Conservation of thermal energy

Figure 13: Relative error in the total thermal energy contained in Ω over time for the case without radiation (left) and the total thermal enery in the domain with and without radiation (right).

In contrast to working with an enthalpy formulation, the mesh moving scheme does not conserve the thermal energy exactly due to the time discretization of Eq. (3d). The actual loss/gain in energy is therefore an aspect in assessing the reliability of the method.

Our numerical experience is that for timestep sizes needed by the rest of the overall scheme, little to no additional refinement is neccessary at the phase boundary to keep the relative error below 0.8 % at all times (see Fig. 13 for an example). The same figure shows the significant influence of radiation on the total thermal energy contained in Ω, which is directly related to the maximum radius of the material accumulation (Fig. 8).

5 Conlusions

We presented an ALE Finite Element Method capable of simulating a melting process with a free capillary surface in a stable and robust manner. The model includes convective heat transfer, radiative cooling at the boundary, phase change, the incompressible viscous flow in the liquid phase and different material data in the two phases, and features a decoupling of the temperature, the velocity and pressure, and the geometry.

Since the grid is moved along with the phase boundary, relatively large mesh deformations can occur, which are cured by occasional remeshings.

Acknowledgements

Appendix

If the dimensional quantities are denoted by an asterisk, we obtain the nondimensional values by setting

$$x = \frac{x^*}{L}, \quad t = \frac{t^*}{\hat{t}}, \quad U = \frac{L}{\hat{t}}, \quad T = \frac{T^* - T_m^*}{T_m^* - T_a^*}, \quad u = \frac{u^*}{U}, \quad p = \frac{p^*}{\rho_l U^2},$$

with the scales $L = 5 \cdot 10^{-3} m$, $\hat{t} = 0.1s$, the ambient and melting point temperatures $T_m^* = 1470K, T_a^* = 293.15K$ and the mass density $\rho_l = 7015 \frac{kg}{m^3}$.

The dimensionless coefficients are the Reynolds, Prandtl, Weber, Bond, Grashof and Stefan numbers

$$Re = \frac{UL\rho_l}{\mu}, \quad Pr = \frac{\mu c_{pl}}{\kappa_l}, \quad We = \frac{\rho_l U^2 L}{\gamma}, \quad Bo = \frac{\rho_l g L^2}{\gamma},$$

$$Gr = \frac{g\beta\rho_l^2(T_m^* - T_a^*)L^3}{\mu^2}, \quad Ste = \frac{c_{pl}(T_m^* - T_a^*)}{\Lambda},$$

and the additional dimensionless parameters for the laser, emissivity, thermal conductivity, mass density and thermal diffusivity

$$La = \frac{I_{max}}{\rho_l c_{pl} U (T_m^* - T_a^*)}, \quad Em = \frac{\varepsilon k_{SB}(T_m^* - T_a^*)^3}{\rho_l c_{pl} U}.$$

$$q_\kappa = \frac{\kappa_s}{\kappa_l}, \quad q_\rho = \frac{\rho_s}{\rho_l}, \quad q_{ls} = \frac{q_\kappa c_{pl}}{q_\rho c_{ps}}, \quad T_a = \frac{T_a^*}{T_m^* - T_a^*}, \quad T_m = \frac{T_m^*}{T_m^* - T_a^*}.$$

These are obtained from the mass densities ρ_l, ρ_s, the specific heat capacities c_{pl}, c_{ps}, the thermal conductivities κ_l, κ_s, the latent heat Λ, the emissivity ε, the maximum laser intensity I_{max}, the dynamic viscosity μ, the surface tension γ, the thermal expansion coefficient β and the Stefan-Boltzmann constant k_{SB}.

Unless stated otherwise, we worked with the values

$$Re = 3, \quad Pr = 0.1, \quad We = 4 \cdot 10^{-5}, \quad Bo = 0.01,$$
$$Gr = 200, \quad La = 10^4, \quad Em = 9 \cdot 10^{-4}, \quad q_\rho = 1.125,$$
$$q_\kappa = 0.4, \quad q_{c_p} = 0.6, \quad T_a = 0.25, \quad T_m = 1.25,$$

as given by the application.

References

[1] A. N. Alexandrou. An inverse finite element method for directly formulated free boundary problems. *International journal for numerical methods in engineering*, 28:2383–2396, 1989.

[2] D. M. Anderson, S. H. Davis, and M. G. Worster. The case for a dynamic contact angle in containerless solidification. *Journal of Crystal Growth*, 163:329–338, 1996.

[3] P. S. Ayyaswami, I. M. Cohen, and L. J. Huang. Melting and solidification of thin wires: A class of phase-change problems with a mobile interface - I. Analysis. *International journal of heat and mass transfer*, 38:1637–1645, 1995.

[4] P. S. Ayyaswami, I. M. Cohen, and S. S. Sripida. Melting of a wire anode followed by solidification: A three-phase moving boundary problem. *Journal of Heat Transfer*, 125:661–668, 2003.

[5] E. Bänsch. Local mesh refinement in 2 and 3 dimensions. *Impact of Computing in Science and Engineering*, 3:181–191, 1991.

[6] E. Bänsch. *Numerical methods for the instationary Navier-Stokes equations with a free capillary surface.* Habilitationsschrift, Universität Freiburg, 1998.

[7] E. Bänsch. Simulation of instationary, incompressible flows. *Acta mathematica Universitatis Comenianae*, 67, no. 1:101–114, 1998.

[8] E. Bänsch. Finite element discretization of the Navier-Stokes equations with a free capillay surface. *Numerische Mathematik*, 88(2):203–235, 2001.

[9] E. Bänsch and A. Schmidt. Simulation of dendritic crystal growth with thermal convection. *Interfaces and Free Boundaries*, 2:95–115, 2000.

[10] S. Basting. *A pdelib2 based Finite Element Implementation and its Application to the Mean Curvature Flow Equation.* Diploma thesis, Universität Erlangen, 2009.

[11] M. O. Bristeau, R. Glowinski, and J. Periaux. Numerical methods for the Navier-Stokes equations. Application to the simulation of compressible and incompressible flows. *Computer Physics Report*, 6:73–188, 1987.

[12] J. Crank. *Free and moving boundary problems.* Clarendon Press, Oxford, 1984.

[13] J. Donea, S. Giuliani, and J. P. Halleux. An arbitrary lagrangian–eulerian finite element method for transient dynamic fluid–structure interactions. *Comp. Meth. Appl. Mech. Engr.*, 33:689–723, 1982.

[14] C. M. Elliot. On the finite element approximation of an elliptic variational inequality arising from an implicit time discretization of the Stefan problem. *IMA Journal of Numerical analysis*, 1:115–125, 1981.

[15] H. Garcke and V. Styles. Bi-directional diffusion induced grain boundary motion with triple junctions. *Interfaces Free Bound.*, 6:271–294, 2004.

[16] R. Griesse and A. J. Meir. Modelling of a magnetohydrodynamics free surface problem arising in Czochralski crystal growth. *Math. Comput. Model. Dyn. Syst.*, 15:163–175, 2009.

[17] N. Malamatris and T. C. Papanastasiou. Analysis of high-speed continuous casting with inverse finite elements. *International journal for numerical methods in fluids*, 13:1207–1223, 1991.

[18] B. Nestler and A. A. Wheeler. A multi-phase-field model of eutectic and peritectic alloys: Numerical simulation of growth structures. *Phys. D*, 138:114–133, 2000.

[19] L. I. Rubinšteĭn. *The Stefan Problem*, volume 27 of *Translations of Mathematical Monographs*. American Mathematical Society, Rhode Island, 1971.

[20] J. R. Shewchuk. Triangle: Engineering a 2D Quality Mesh Generator and Delaunay Triangulator. In M. C. Lin and D. Manocha, editors, *Applied Computational Geometry: Towards Geometric Engineering*, volume 1148 of *Lecture Notes in Computer Science*, pages 203–222. Springer-Verlag, May 1996. From the First ACM Workshop on Applied Computational Geometry.

[21] A. E. Siegman. *Lasers*. University Science Books, Mill Valley, California, 1986.

[22] F. Vollertsen and R. Walther. Energy balance in laser based free form heading. *CIRP Annals*, 57:291–294, 2008.

E. Bänsch and J. Paul: AM III, Department Mathematics, University of Erlangen, Germany; A. Schmidt: ZeTeM, FB 3, University of Bremen, Germany.